The Astrophysical Journal, 886:145 (14pp), 2019 December 1 https://doi.org/10.3847/1538-4357/ab5110

The Nature of the Broadband X-Ray Variability in the Dwarf Seyfert Galaxy NGC 4395

E. S. Kammoun[1], E. Nardini[2], A. Zoghbi[1], J. M. Miller[1], E. M. Cackett[3], E. Gallo[1], M. T. Reynolds[1], G. Risaliti[2,4], D. Barret[5], W. N. Brandt[6,7,8], L. W. Brenneman[9], J. S. Kaastra[10,11], M. Koss[12], A. M. Lohfink[13], R. F. Mushotzky[14], J. Raymond[9], and D. Stern[15]

[1] Department of Astronomy, University of Michigan, 1085 South University Avenue, Ann Arbor, MI 48109-1107, USA; ekammoun@umich.edu
[2] INAF—Osservatorio Astrofisico di Arcetri, Largo Enrico Fermi 5, I-50125 Firenze, Italy
[3] Department of Physics & Astronomy, Wayne State University, 666 W. Hancock Street, Detroit, MI 48201, USA
[4] Dipartimento di Fisica e Astronomia, Università di Firenze, Via G. Sansone 1, I-50019 Sesto Fiorentino (Firenze), Italy
[5] IRAP, Université de Toulouse, CNRS, UPS, CNES, 9, Avenue du Colonel Roche, BP 44346, F-31028 Toulouse Cedex 4, France
[6] Department of Astronomy and Astrophysics, 525 Davey Lab, The Pennsylvania State University, University Park, PA 16802, USA
[7] Institute for Gravitation and the Cosmos, The Pennsylvania State University, University Park, PA 16802, USA
[8] Department of Physics, 104 Davey Lab, The Pennsylvania State University, University Park, PA 16802, USA
[9] Harvard-Smithsonian Center for Astrophysics, 60 Garden Street, Cambridge, MA 02138, USA
[10] SRON Netherlands Institute for Space Research, Sorbonnelaan 2, 3584 CA Utrecht, The Netherlands
[11] Leiden Observatory, Leiden University, P.O. Box 9513, 2300 RA Leiden, The Netherlands
[12] Eureka Scientific, 2452 Delmer Street Suite 100, Oakland, CA 94602-3017, USA
[13] Montana State University, P.O. Box 173840, Bozeman, MT 59717-3840, USA
[14] Department of Astronomy and Joint Space-Science Institute, University of Maryland, College Park, MD 20742, USA
[15] Jet Propulsion Laboratory, California Institute of Technology, 4800 Oak Grove Drive, MS 169-221, Pasadena, CA 91109, USA
Received 2019 July 22; revised 2019 October 23; accepted 2019 October 23; published 2019 December 3

Abstract

We present a flux-resolved X-ray analysis of the dwarf Seyfert 1.8 galaxy NGC 4395, based on three archival *XMM-Newton* and one archival *NuSTAR* observations. The source is known to harbor a low-mass black hole ($\sim 10^4$–a few $\times\ 10^5\ M_\odot$) and shows strong variability in the full X-ray range during these observations. We model the flux-resolved spectra of the source assuming three absorbing layers: neutral, mildly ionized, and highly ionized ($N_{\rm H} \sim 1.6 \times 10^{22}$–$3.4 \times 10^{23}\ {\rm cm}^{-2}$, ~ 0.8–$7.8 \times 10^{22}\ {\rm cm}^{-2}$, and $3.8 \times 10^{22}\ {\rm cm}^{-2}$, respectively). The source also shows intrinsic variability by a factor of ~ 3 on short timescales, which is due to changes in the nuclear flux, assumed to be a power law ($\Gamma = 1.6$–1.67). Our results show a positive correlation between the intrinsic flux and the absorbers' ionization parameter. The covering fraction of the neutral absorber varies during the first *XMM-Newton* observation, which could explain the pronounced soft X-ray variability. However, the source remains fully covered by this layer during the other two observations, largely suppressing the soft X-ray variability. This suggests an inhomogeneous and layered structure in the broad-line region. We also find a difference in the characteristic timescale of the power spectra between different energy ranges and observations. We finally show simulated spectra with *XRISM*, *eXTP*, and *Athena*, which will allow us to characterize the different absorbers, study their dynamics, and will help us identify their locations and sizes.

Unified Astronomy Thesaurus concepts: Active galactic nuclei (16); Seyfert galaxies (1447); High energy astrophysics (739); X-ray active galactic nuclei (2035); X-ray astronomy (1810); Intermediate-mass black holes (816); Astrophysical black holes (98); Supermassive black holes (1663); Low-luminosity active galactic nuclei (2033)

1. Introduction

The dwarf Seyfert 1.8 galaxy NGC 4395 ($d = 4.2$ Mpc; Karachentsev & Drozdovsky 1998) is one of the most X-ray variable non-jetted active galactic nuclei (AGNs; e.g., Iwasawa et al. 2000; Vaughan et al. 2005; Iwasawa et al. 2010). The optical and ultraviolet (UV) spectra of this source show high-ionization forbidden lines with broad wings corresponding to gas velocities higher than $\sim 10^3\ {\rm km\ s^{-1}}$ (Filippenko & Sargent 1989), in addition to permitted lines such as C IV, Mg II, O III, and Hα (see, e.g., Filippenko et al. 1993). Peterson et al. (2005) obtained a mass of $M_{\rm BH} = (3.6 \pm 1.1) \times 10^5\ M_\odot$, based on reverberation mapping of C IV. More recently, Woo et al. (2019) estimated the time delay in the Hα band to be 83 ± 14 minutes and found a small velocity dispersion of $\sigma_{\rm H\alpha} = 426 \pm 1\ {\rm km\ s^{-1}}$, inferring an even lower mass of $M_{\rm BH} = 9.1^{+1.5}_{-1.6} \times 10^3\ M_\odot$. The source can thus be considered to lie at the highest end of the still-elusive intermediate-mass black hole (BH) population (see, e.g., Koliopanos et al. 2017; Mezcua et al. 2018, and references therein), representing a scaled-down (by ~ 2 orders of magnitude) version of ordinary and more luminous Seyfert galaxies.

X-ray observations of NGC 4395 revealed strong variability in the soft X-rays (below ~ 2 keV) that have been attributed to a complex multizone ionized absorber (e.g., Iwasawa et al. 2000; Dewangan et al. 2008). Nardini & Risaliti (2011; hereafter NR11) studied the time-resolved spectra obtained from two long observations with *XMM-Newton* and *Suzaku* with the aim of explaining the anomalously flat X-ray spectrum of NGC 4395 (see, e.g., Moran et al. 2005). They found that the source exhibited partial occultation by cold material with column densities $N_{\rm H} \sim 10^{22}$–$10^{23}\ {\rm cm}^{-2}$, consistent with a clumpy broad-line region. These results were later confirmed by Parker et al. (2015), who studied the X-ray variability of this source applying a principle component analysis (PCA) to the *XMM-Newton* data. Their results show that the variability in NGC 4395 is accounted for by a combination of intrinsic flux variability and changes in the absorption covering fraction, with hints of changes also in the column density of the

absorbing material. The X-ray spectra of this source show a prominent narrow Fe K line, attributed to neutral reflection by distant material (e.g., Iwasawa et al. 2000, 2010, NR11). This is consistent with the PCA that did not show any hint of reflection variability. This was also confirmed by Kara et al. (2016), who did not detect any evidence of low-frequency hard lag or Fe K lags from all three *XMM-Newton* observations, despite the fact that De Marco et al. (2013) have detected hints of soft lags using the first *XMM-Newton* observation only. We note that these lags could potentially be produced by reprocessing from the warm absorber(s), as shown by Silva et al. (2016) for NGC 4051.

In this work, we analyze the flux-resolved spectra of three *XMM-Newton* observations (including the one studied by NR11) in addition to a short *NuSTAR* observation. Observations and data reduction are described in Section 2. The spectral analysis is presented in Section 4. In Section 3 we show the fractional rms variability obtained from the different observations, in addition to the power spectral density (PSD) using the *XMM-Newton* observations. Finally, we discuss the results in Section 5, and we present our conclusions in Section 7.

2. Observations and Data Reduction

2.1. XMM-Newton *Observations*

NGC 4395 was observed by *XMM-Newton* (Jansen et al. 2001) on 2003 November 30 (Obs ID 0142830101, hereafter Obs. 1), for a total duration of ∼113 ks. The time-resolved spectra from this observation have been presented by NR11. The source was later observed on 2014 December 28 and 30 (Obs IDs 0744010101 and 0744010201, hereafter Obs. 2+3, respectively) for a duration of ∼53 ks each. We reduced the data from the three observations using `SAS v.17.0.0` (Gabriel et al. 2004) and the latest calibration files. We followed the standard procedure for reducing the data of the EPIC-pn (Strüder et al. 2001) CCD camera, operating in full-frame mode for Obs. 1 and small-window mode for Obs. 2+3, with medium filter. The data were processed using EPPROC. Source spectra and light curves were extracted from a circular region with a radius of 30″ for all observations. The corresponding background spectra and light curves were extracted from an off-source circular region located on the same chip, with a radius approximately twice that of the source. After filtering out periods with strong background flares, the net exposure times dropped to 88.7 ks, 36.2 ks, and 22.5 ks for Obs. 1, 2, and 3, respectively.

The light curves were produced using the `SAS` task `EPICLCCORR`. Figure 1 shows the 0.5–2 and 2–10 keV light curves for the three observations, clearly revealing the large variability of this source. We note that in Obs. 1 the source was significantly brighter and more variable in the 0.5–2 keV range than in Obs. 2 and 3, while it shows a similar brightness and variability amplitude for all observations in the 2–10 keV band. Given the consistency between Obs. 2 and Obs. 3, and in order to increase the signal-to-noise ratio (S/N), we combine the two observations (hereafter Obs. 2+3) in the rest of this work.

2.2. NuSTAR *Observations*

NuSTAR (Harrison et al. 2013) observed NGC 4395 for a net exposure of 19 ks on 2013 May 10. The data were reduced using the standard pipeline in the *NuSTAR* Data Analysis Software (`NUSTARDAS` v1.8.0), and using the latest calibration files. We cleaned the unfiltered event files with the standard depth correction. We reprocessed the data using the `saamode = optimized` and `tentacle = yes` criteria for a more conservative treatment of the high background levels in the proximity of the South Atlantic Anomaly. We extracted the source and background light curves and spectra from circular regions of radii 60″ and 120″, respectively, for the two focal plane modules (FPMA and FPMB) using the `HEASOFT` task `nuproducts`.

We added the FPMA and FPMB light curves using the `FTOOLS` (Blackburn 1995) command `LCMATH`. Figure 2 shows the background-subtracted light curves in the 4–10 and 10–30 keV bands with a time bin of 1 ks. The source varies simultaneously in both energy bands on the timescales probed by the observations.

3. Timing Analysis

In this section we investigate the variability seen in NGC 4395 through two model-independent approaches. First, we present the fractional rms variability amplitude ($F_{\rm var}$) for the various observations. Then we analyze the PSD for the various *XMM-Newton* observations.

3.1. Fractional Variability

It is clear from Figures 1 and 2 that the source is highly variable in all energy ranges. We characterize the variability by estimating $F_{\rm var}$ and its corresponding error, following Vaughan et al. (2003). We estimate $F_{\rm var}$ from the 1 ks binned light curves of all observations in various energy bands, as shown in Figure 3. The segment lengths that are used to estimate $F_{\rm var}$ are 103 ks, 97 ks, and 37 ks for Obs. 1, 2+3, and *NuSTAR*, respectively, corresponding to the full observation lengths, after filtering. We note that due to the low flux and the low variability level below ∼1 keV in Obs. 2+3 compared with Obs. 1, it was not possible to estimate $F_{\rm var}$ in small energy bins. For that reason, we limit our analysis to one bin in the 0.4–1 keV range.

Figure 3 shows that $F_{\rm var}$ is constant ($\langle F_{\rm var}\rangle \simeq 0.28$) above 5 keV for all observations. This indicates that the variability in this range is mainly due to variations in the intrinsic flux of the nuclear emission (assumed to have a power-law shape varying in normalization only) in each observation. Some deviations, though not statistically significant, can be seen in the 6–7 and 15–20 keV ranges, where the relative contribution of reflection features (Fe K emission line and Compton hump, respectively) is expected to be larger. Longer *NuSTAR* observations would be needed to confirm the presence of these features, especially above 10 keV. However, $F_{\rm var}$ increases below ∼4 keV in Obs. 1, reaching more than ∼0.9. This could be mainly due to the complex variable absorption structure in this source affecting mainly the soft X-rays (see NR11 and Section 4 in the current work, for more details about the spectral modeling). Intrinsic variability due to a change in the flux of the power-law component would result in a nearly constant $F_{\rm var}$ at all energies. However, any additional variability process that might be caused by a change in absorption, for example, would lead to an increase in the values of $F_{\rm var}$ in the energy range affected by these changes (see, e.g., Matzeu et al. 2016, and Section 5 for more details). We note that that this does not necessarily imply

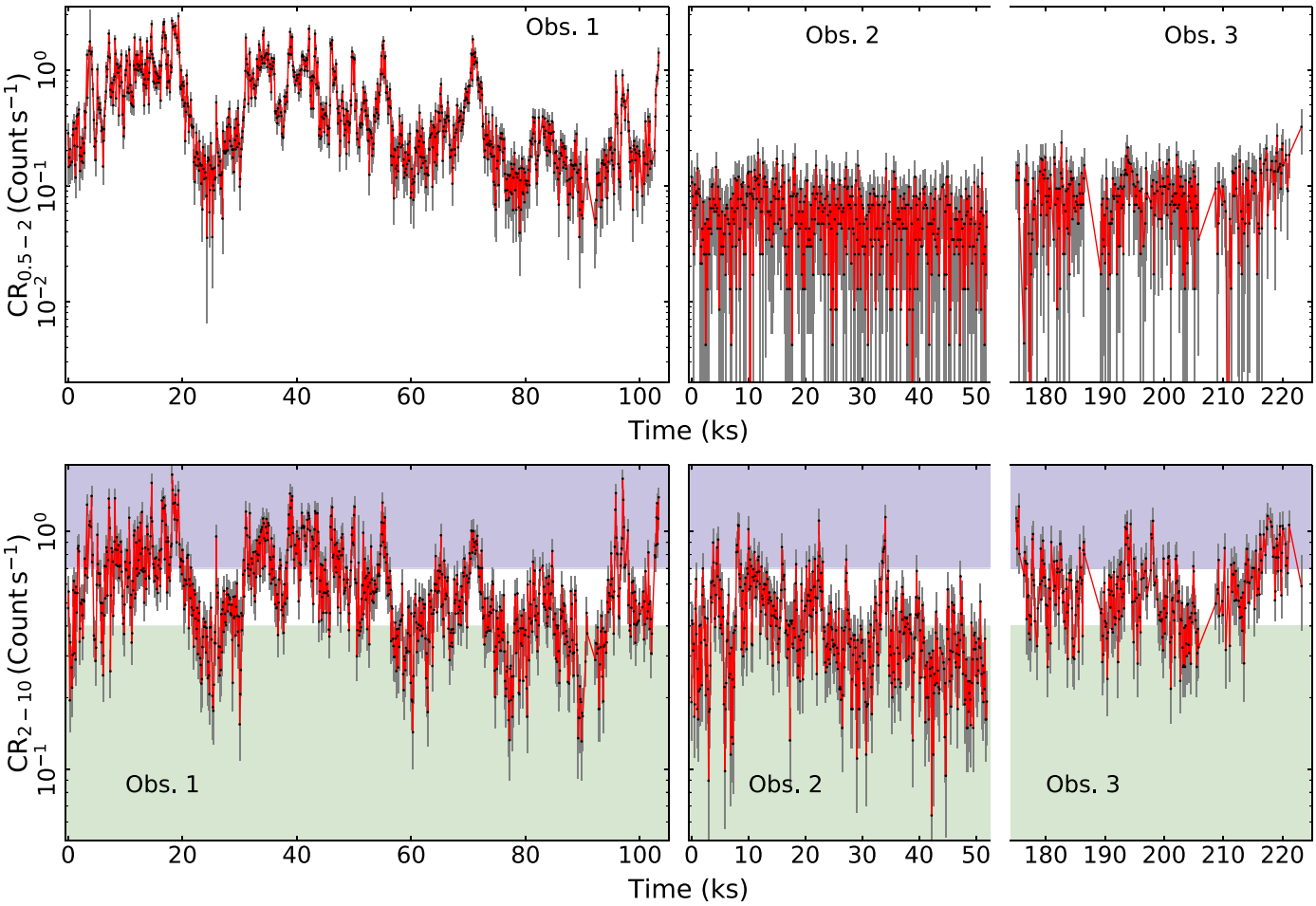

Figure 1. Background-subtracted *XMM-Newton* light curves in the 0.5–2 keV (top panel) and 2–10 keV (bottom panel) bands, with a time bin of 100 s. The time in Obs. 3 is from the start of Obs. 2. The green, white, and blue areas correspond to the low-, medium-, and high-flux levels considered in this work (see Section 4 for details).

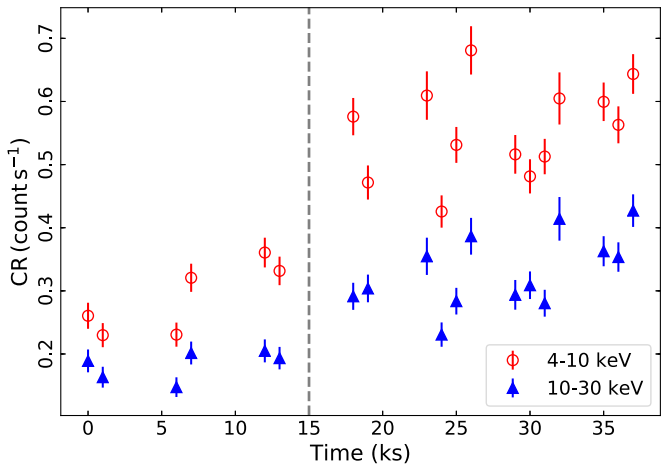

Figure 2. Background-subtracted *NuSTAR* light curves in the 4–10 keV (open circles) and 10–30 keV (filled triangles) bands, with a time bin of 1 ks and an exposure fraction >0.5. The light curves of FPMA and FPMB are added together. The medium- and high-flux spectra are extracted from times before and after the flux increase at ∼15 ks (dashed vertical line; see see Section 4 for details).

that the intrinsic continuum fluctuations and the absorption changes contributing to the variability in the soft X-rays are operating on the same timescales. Any changes in the absorber column density and/or the covering fraction are expected to occur on longer timescales than the continuum. Hence, what drives the increase in $F_{\rm var}$ is the large amplitude (a factor of more than 30 compared to ∼3 below and above 2 keV, respectively, as seen in Figure 1) of the variations associated with such changes. As for Obs. 2+3, $F_{\rm var}$ is zero in the 0.4–1 keV, indicating a low variability amplitude in this energy range.

3.2. The Power Spectral Density

As an additional model-independent variability study, we estimate the PSD of the source in different energy bands, using the periodogram (e.g., Vaughan et al. 2003). Background-subtracted light curves with a sampling time of 16 s are extracted from standard event files as described in Section 2.1. Gaps smaller than 400 s resulting from the standard background filtering are linearly interpolated and randomized. The periodogram using the rms normalization (see Vaughan et al. 2003) is then calculated from the discrete Fourier transform of the light curve arrays. The final periodogram is produced by averaging every 20 frequency values. The modeling is done in XSPEC using the Whittle20 statistic (Whittle 1953; Vaughan 2010; Barret & Vaughan 2012). A simple power law does not account for the apparent break at ∼a few $\times 10^{-4}$ Hz (see Vaughan et al. 2005). Hence, to estimate the characteristic timescale, the periodograms are modeled with a zero-centered

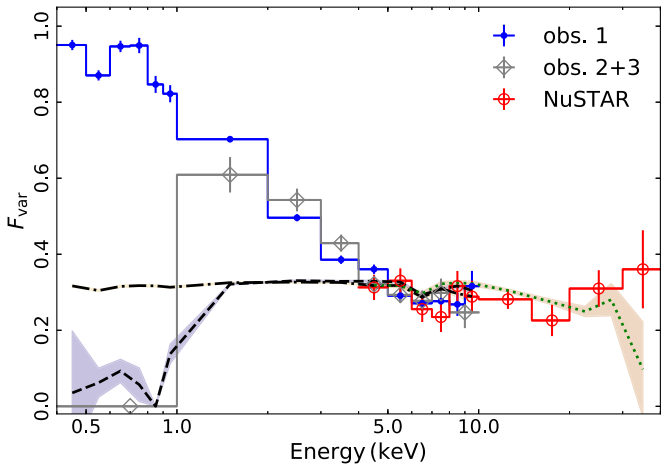

Figure 3. The fractional rms variability amplitude (F_{var}) as a function of energy, obtained from the light curves, with a time bin of 1 ks, of Obs. 1 (blue dots), Obs. 2+3 (gray diamonds), and the *NuSTAR* observation (open red circles). The black dash–dotted line corresponds to simulated F_{var}, using *XMM-Newton* responses, assuming an unabsorbed power law varying in normalization only. The black dashed line and the green dotted line correspond to simulated F_{var}, using *XMM-Newton* and *NuSTAR* responses, respectively, assuming an absorbed power law varying in normalization only. The column density and covering fraction of the absorber are constant and consistent with the best-fit values obtained from Obs. 2+3. The shaded areas correspond to the 1σ uncertainty on the simulated F_{var} (see Section 5 for more details about the simulations). The simulated F_{var} are in agreement with the observations above 4 keV, while they could not reproduce the observed variability at softer energies.

Lorentzian of the form

$$P(\nu) = K\frac{\sigma}{2\pi}\frac{1}{\nu^2 + (\sigma/2)^2}, \quad (1)$$

where K is the normalization. In the $\nu P(\nu)$ representation, the peak frequency $\nu_{peak} = \sigma/2$ can be considered as the characteristic frequency of the PSD (see e.g., Belloni et al. 1997, 2002). The Poisson noise is modeled with a constant for each PSD. The errors on the model parameters are estimated using the Goodman–Weare Markov chain Monte Carlo (MCMC) algorithm in XSPEC (Goodman & Weare 2010). We estimate the PSDs separately from Obs. 1 and Obs. 2+3 (combined together). The top panel of Figure 4 shows the PSD of NGC 4395 in the 0.3–2, 2–5 and 5–10 keV bands. The best-fit σ and normalization of the Lorentzian are listed in Table 1.

The probability densities of σ for each case are shown in the lower panel of Figure 4. This figure shows that the characteristic frequency is lower in Obs. 1 than in Obs. 2+3 for all energy bands. Furthermore, the values of σ in the 0.3–2 and 2–5 keV bands are consistent during Obs. 1, and lower than the best-fit value in the 5–10 keV band. This behavior could be due to the fact that Obs. 1 is affected by both intrinsic variability and an additional variability process, most probably absorption changes (as discussed in NR11 and Section 4.1 of the current work), though operating on different timescales. The additional variability process, also seen in the F_{var}, is expected to occur on timescales that are longer than the intrinsic variability, and to affect mainly the soft X-rays. Hence, its contribution to the overall variability decreases as the energy increases, which might explain the shift to shorter timescales in Obs. 1 as the intrinsic variability becomes more dominant (in the hard X-rays). However, in Obs. 2+3, the intrinsic variability seems to be dominating all energy bands, which could explain the fact that the values of σ are consistent over the full 0.3–10 keV range. We note that the apparent high value of σ in the 0.3–2 keV band in Obs. 2+3 is mainly due to the data quality because signal is heavily affected by the Poisson noise. The value of σ in the 5–10 keV range in Obs. 1 is systematically lower than the one in Obs. 2+3 (they are consistent within $\sim 2.5\sigma$). This is most likely due to the relatively high column density of the variable neutral absorber in Obs. 1 (as discussed in Section 4.1), which still affects the overall variability in this energy range (though in a more moderate way), shifting the characteristic timescale toward a slightly higher value.

It is known that the power-spectrum break timescale, BH mass, and X-ray luminosity established for unobscured AGN and Galactic BH systems are related by

$$\log T_B = 2.1\log(M_{BH,6}) - 0.98\log(L_{bol,44}) - 2.32, \quad (2)$$

$$\log T_B = 1.39\log(M_{BH,6}) - 0.82\log(L_{bol,44}) - 2.7, \quad (3)$$

as derived by McHardy et al. (2006) and González-Martín (2018), respectively. In both relationships, T_B is the break timescale in units of day, $M_{BH,6}$ is the BH mass in units of $10^6\,M_\odot$, and $L_{bol,44}$ is the bolometric luminosity in units of 10^{44} erg s^{-1}. We note that in our modeling we do not assume a broken shape of the PSD. If these relationships hold also for NGC 4395, then considering $T_B = \nu_{peak}^{-1} = (\sigma/2)^{-1}$, with $\sigma = 1.9$ mHz (considering mainly the intrinsic variability above 5 keV in Obs. 2+3; see Table 5), and a bolometric luminosity[16] of 1.52×10^{41} erg s^{-1}, we infer $M_{BH} = 8.4 \times 10^4\,M_\odot$ and $9.2 \times 10^4\,M_\odot$, following Equations (2) and (3), respectively. González-Martín (2018) also showed that obscuration events might affect the T_B–M_{BH} relationship. Our mass estimate is intermediate compared to the previously reported estimates of $9.1^{+1.5}_{-1.6} \times 10^3\,M_\odot$ (Woo et al. 2019) and $(3.6 \pm 1.1) \times 10^5\,M_\odot$ (Peterson et al. 2005). It is worth mentioning that this bolometric luminosity would correspond to an Eddington ratio $L_{bol}/L_{Edd} = 0.12\,(0.003)$ for $M_{BH} = 10^4\,(3.6 \times 10^5)\,M_\odot$.

4. X-Ray Spectral Analysis

Following a complementary approach with respect to the time-resolved analysis of NR11, here we consider the flux-resolved spectra from all observations. For *XMM-Newton*, we extract the spectra for three different flux levels, using the EPIC-pn light curves: low, medium, and high, with a 2–10 keV count rate below 0.4 count s^{-1}, between 0.4 count s^{-1} and 0.7 count s^{-1}, and above 0.7 count s^{-1}, respectively (as shown in Figure 1). The *XMM-Newton* spectra from the different flux levels and observations are grouped requiring a minimum S/N of 4 per energy bin. We have also checked the EPIC-MOS data. The data from Obs. 3 are heavily affected by background flares and cannot be used. Moreover, matching the count rates between the various detectors to define the flux states is not trivial, and adding the MOS spectra would be of a little help in the low-flux states due to the poor data quality, and it would be redundant for the high-flux levels. Hence, for simplicity, we

[16] Lira et al. (1999) estimated $L_{bol} = 1.2 \times 10^{41}$ erg s^{-1} for $d = 5.2$ Mpc and considering the spectral energy distribution below 2 keV. However, for $d = 4.2$ Mpc (Karachentsev & Drozdovsky 1998). Adding the 2–100 keV luminosity assuming the best-fit from the medium-flux *NuSTAR* spectrum (see Section 4.1), we obtain $L_{bol} = 1.91 \times 10^{41}$ erg s^{-1}.

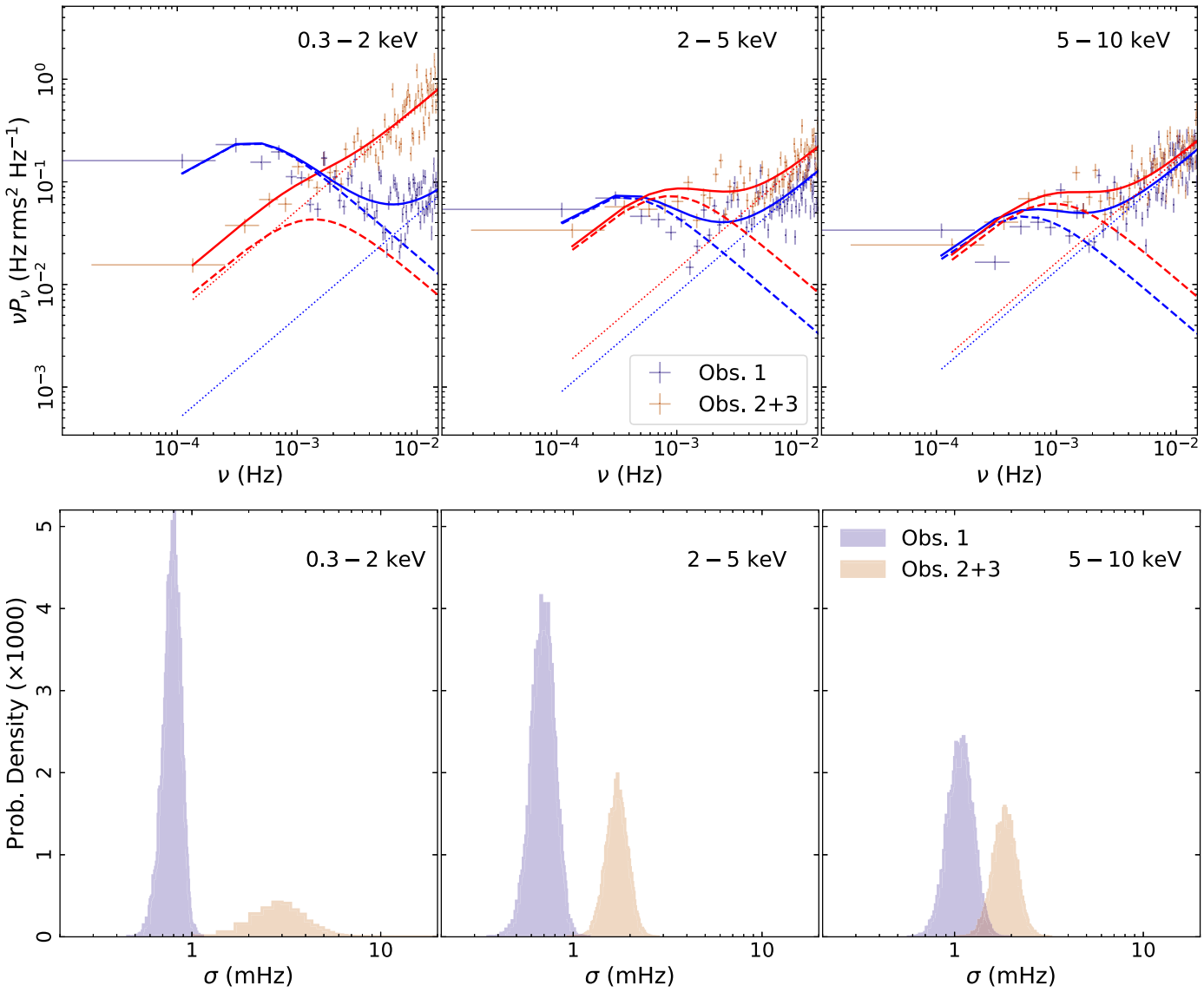

Figure 4. Top panel: power spectral density for Obs. 1 (blue) and Obs. 2+3 (red) in the 0.3–2, 2–5, and 2–10 keV bands. The solid lines show the best-fit models, the dashed lines correspond to the best-fit Lorentzian, the dotted lines represent the Poisson noise level. Bottom panel: the probability density of double the characteristic frequency ($\sigma = 2\nu_{\rm peak}$) for each case, obtained from the MCMC analysis (see Section 3.2 for details).

decided to neglect the MOS data. We also checked the RGS data. However, they are dominated by noise, even when the time-averaged spectra are considered. For this reason we do not include them in this analysis.

The *NuSTAR* light curves presented in Figure 2 show an increase in flux after ∼15 ks from the start of the observation. Thus, we extract spectra before and after the flux increase at 15 ks, requiring a minimum S/N of 4 per energy bin. The spectra extracted from FPMA and FPMB (extending up to 70 keV) are consistent with each other for both flux levels, so they are analyzed jointly (but not combined together). Table 2 shows the net count rate (in the 0.5–3 and 3–10 keV bands) and the net exposure time for each flux level in the different observations. The spectra from all flux levels are shown in Figure 5. It can be seen that the soft X-rays (below ∼1 keV) vary by a factor of more than ∼6 in Obs. 1 (between the low- and high-flux levels) while they are consistent with each other for all flux levels in Obs. 2+3. The spectra from all flux levels in Obs. 1 and 2+3 are consistent above ∼4 keV. As for the *NuSTAR* observation, the spectra extracted from the first part of the observation are consistent with the medium-flux spectra extracted from the *XMM-Newton* observations, and the spectra

Table 1
The Best-fit σ and Normalization Obtained by Fitting the PSDs with a Lorentzian Function in the 0.3–2, 2–5, and 2–10 keV Bands

	Obs. 1	Obs. 2+3
	0.5–2 keV	
σ (mHz)	0.79 ± 0.08	$3.43^{+0.57}_{-1.40}$
Norm ($\times 10^{-1}$)	$7.59^{+0.51}_{-0.81}$	$1.48^{+0.23}_{-0.35}$
	2–5 keV	
σ (mHz)	$0.71^{+0.09}_{-0.11}$	$1.74^{+0.21}_{-0.24}$
Norm ($\times 10^{-1}$)	$2.26^{+0.19}_{-0.26}$	$2.30^{+0.16}_{-0.20}$
	5–10 keV	
σ (mHz)	$1.11^{+0.15}_{-0.18}$	$1.90^{+0.23}_{-0.30}$
Norm ($\times 10^{-1}$)	$1.46^{+0.11}_{-0.15}$	$1.96^{+0.15}_{-0.17}$

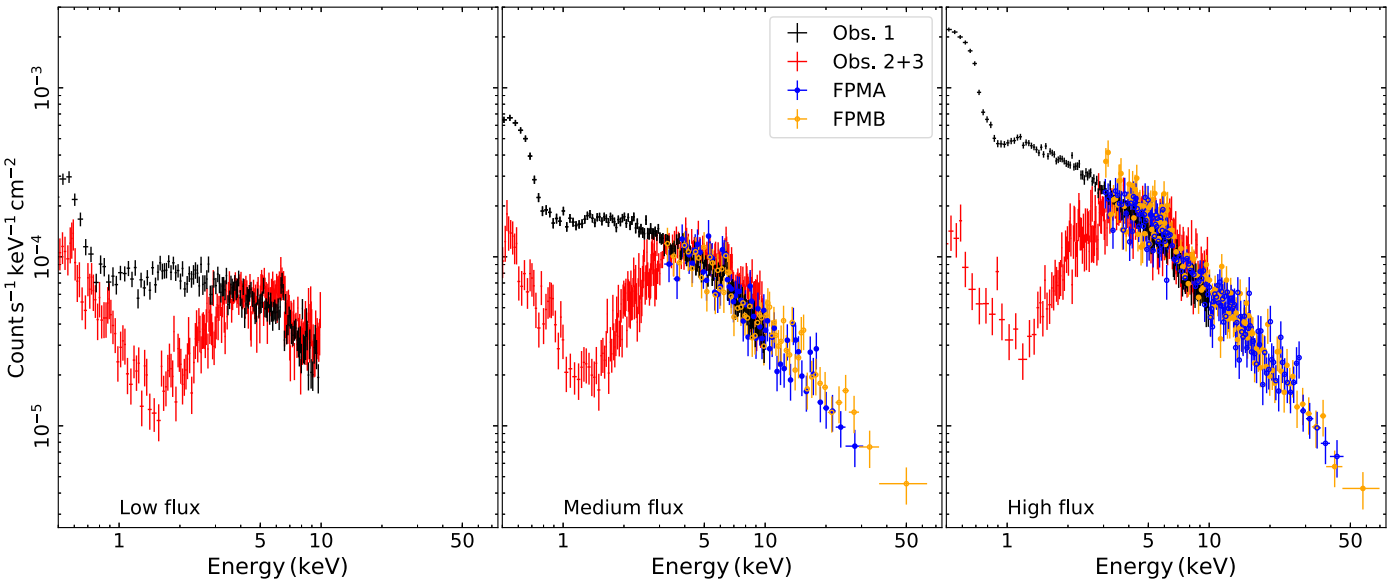

Figure 5. Low-, medium-, and high-flux spectra (left, middle, and right panel) from Obs. 1 (black), Obs. 2+3 (red), and the *NuSTAR* observation (FPMA and FPMB in blue and orange dots, respectively).

Table 2
Net Count Rate (in the 0.5–3 and 3–10 keV Bands) and Net Exposure Time for Each Flux-resolved Spectrum Obtained from the Different Observations

	Low	Mean	High
Obs. 1			
$CR_{0.5-3}$	0.202 ± 0.003	0.435 ± 0.004	1.131 ± 0.007
CR_{3-10}	0.199 ± 0.003	0.331 ± 0.003	0.55 ± 0.005
Net exposure	23.3	38.9	26.5
Osb. 2+3			
$CR_{0.5-3}$	0.076 ± 0.002	0.113 ± 0.002	0.199 ± 0.005
CR_{3-10}	0.215 ± 0.003	0.384 ± 0.004	0.598 ± 0.009
Net exposure	24.8	25.2	8.7
NuSTAR/FPMA			
CR_{3-10}	···	0.126 ± 0.004	0.218 ± 0.004
Net exposure (ks)	···	6.9	12
NuSTAR/FPMB			
CR_{3-10}	···	0.113 ± 0.004	0.224 ± 0.004
Net exposure	···	6.9	12

Note. Count rates are in units of count s^{-1}, exposure times are in units of ks.

from the second part of the observation are consistent with the high-flux *XMM-Newton* spectra.

Throughout this work, spectral fitting is performed using XSPEC v12.10e (Arnaud 1996). The *XMM-Newton* spectra are fit in the 0.5–10 keV range, while the *NuSTAR* spectra are fit in the 3–70 keV range. We apply the χ^2 statistic using the "model" weighting. This weighting method estimates errors on each bin based on the model-predicted number of counts rather than on the square root of the number of counts, which can introduce a bias in the fit to low-flux states at modest count rates. We list the uncertainties on the parameters at the 90% confidence level ($\Delta\chi^2 = 2.71$), unless stated otherwise. These uncertainties are calculated from an MCMC[17] analysis, starting from the best-fitting model that we obtained. We used the Goodman–Weare algorithm (Goodman & Weare 2010) with a chain of 5×10^5 elements, discarding the first 30% of elements as part of the burn-in period.

4.1. Spectral Fitting

Previous studies (e.g., Iwasawa et al. 2000; Dewangan et al. 2008; Iwasawa et al. 2010, NR11) show that the X-ray spectrum of NGC 4395 is composed of a primary power-law continuum that is affected by complex neutral and ionized absorption, in addition to a neutral reflection component. Moreover, the *Chandra* and the *Hubble Space Telescope* (*HST*) [O III] images of the source (see, e.g., Gómez-Guijarro et al. 2017) show an extended soft-emission region. Hence, we fit the spectra using a power-law model with a high-energy cutoff, modified by neutral and ionized partial covering absorbers. We also added a neutral reflection component and an emission component from a collisionally ionized diffuse gas representing the contribution from the extended regions. The model is written in XSPEC terminology as follows:

$$\texttt{M1} = \texttt{phabs[1]} * (\texttt{zpcfabs[2]} * \texttt{zxipcf[3]} * \texttt{zcutoffpl[4]} + \texttt{pexmon[5]} + \texttt{apec[6]}), \quad (4)$$

where `phabs[1]` accounts for Galactic absorption in the line of sight (LOS) of the source ($N_{\rm H} = 4.34 \times 10^{20}$ cm^{-2}; HI4PI Collaboration et al. 2016) and `zpcfabs[2]`, `zxipcf[3]` (Reeves et al. 2008) account for the neutral and ionized absorption, respectively, at the redshift of the source. Neutral reflection is modeled using `pexmon[5]`[18] (Nandra et al. 2007), and diffuse emission is modeled using `apec[6]` (Smith et al. 2001).

We kept the photon index of `cutoffpl` as a free parameter for Obs. 1 but tied among the three flux levels. For the rest of the observations (Obs. 2+3 and *NuSTAR*), we kept Γ tied to a

[17] We use the `XSPEC_EMCEE` implementation of the `PYTHON EMCEE` package for X-ray spectral fitting in `XSPEC` by Jeremy Sanders (http://github.com/jeremysanders/xspec_emcee).

[18] The data do not require any ionized reflection. Hence, using a different model for the reflection, such as `Xillver` (García & Kallman 2010; García et al. 2013), which includes emission lines from more elements than `pexmon`, would not affect our results because the contribution of these emission lines to the soft spectrum would be negligible for neutral reflection.

single free value jointly determined by the flux-selected spectra. We fixed the high-energy cutoff to 500 keV and let the normalization be free for all the spectra. For the `pexmon` model we linked the photon index and high-energy cutoff to the corresponding `cutoffpl` parameters. We fixed the abundance to the solar value and the inclination to 45°. The normalization of `pexmon` is free for Obs. 1 and Obs. 2+3 (tied among the three flux levels).[19] The temperature and the normalization of the `apec` component are kept tied for all observations and flux levels.

We let the column density of the neutral absorber ($N_{\rm H,N}$) and the corresponding covering fractions be free for all of the spectra. As for the *NuSTAR* spectra, due to the lack of a simultaneous high-quality observation in the soft X-rays, it is hard to identify and characterize all the possible absorption components. Hence, we conservatively assume that neutral absorption fully covers the source. Fitting the *NuSTAR* data for ionized absorption resulted in unconstrained parameters and a covering fraction consistent with zero. For this reason we do not consider this component in the fit. The fit also suggested a fully covering neutral absorber for Obs. 2+3 with a constant $N_{\rm H,N}$ across all flux levels. Therefore we fixed the neutral covering fraction to 1 and tied $N_{\rm H,N}$ for all flux levels. For Obs. 1, the fit suggests a variable covering fraction among the different flux levels. As for the ionized absorber, we kept the column densities ($N_{\rm H,W1}$) and the corresponding covering fractions free to vary between observations, but tied for the different flux levels. However, we left the ionization parameter[20] ($\log \xi_{\rm W1}$) free to vary for all of the spectra. The resulting fit is not statistically acceptable ($\chi^2/{\rm dof} = 1775/1537$) with residuals suggesting absorption-like features in the 0.6–1 keV range, as seen in the top panel of Figure 6.

Hence, we added another ionized absorption component at the redshift of the source, also modeled with `zxipcf`, to account for an absorber with a higher ionization level than the absorber we probed before. The model becomes, in XSPEC terminology,

```
M2 = phabs[1]*
(zpcfabs[2] * zxipcf[3] * zxipcf[4]
*zcutoffpl[5] + pexmon[6] + apec[7]).        (5)
```

For `M2` we kept the column density ($N_{\rm H,W2}$), the ionization parameter ($\log \xi_{\rm W2}$), and the covering fraction (${\rm CF_{W2}}$) free to vary between Obs. 1 and the other observations. We kept $N_{\rm H,W2}$ and ${\rm CF_{W2}}$ tied for the different flux levels corresponding to the same observations, and $\log \xi_{\rm W2}$ free to vary between the flux levels. The covering fractions for Obs. 2+3 and the *NuSTAR* observation were consistent with zero, so we do not consider the presence of this component for these observations. The fit is still not statistically acceptable ($\chi^2/{\rm dof} = 1684/1532$), but it has improved by $\Delta\chi^2 = -91$ for five more free parameters. The improvement in Obs. 1 can be clearly seen in the second row of Figure 6. Some excess emission in the ∼0.6–1.5 keV range is still seen in Obs. 2+3. This component could be accounted for by the temperature gradient that is expected to be present in the diffuse gas. For this reason, and for consistency with our previous modeling, we added another `apec` component that is conservatively assumed to be constant for all observations. The model becomes

```
M3 = phabs[1]*
(zpcfabs[2] * zxipcf[3] * zxipcf[4]
*zcutoffpl[5] + pexmon[6] + apec[7] + apec[8])
                                             (6)
```

The fit is statistically acceptable ($\chi^2/{\rm dof} = 1568/1530$, $p_{\rm null} = 0.24$) with $\Delta\chi^2 = -116$ for two more free parameters. The residuals shown in the third row of Figure 6 and the bottom rows of Figure 7 show a clear improvement in all observations with no obvious residuals.

The best-fit model and all components are presented in Figure 7. We report in Tables 3 and 4 the best-fit parameters for the absorption and emission components, respectively. The best fits reveal a small change in the power-law photon index from $1.67^{+0.02}_{-0.04}$ in Obs. 1 to 1.60 ± 0.04 in the other observations. We note that letting the photon index vary among the various flux levels resulted in consistent results. It is also clear that max-to-min variability due to the change in the power-law flux is ∼2.4 on average, while the rest of the spectral variability, observed in the soft X-rays, is driven by the absorption changes. In fact, in Obs. 1, the neutral and the ionized absorbers are variable. The different flux states, during this observation, require an $N_{\rm H,N} = 34.4^{+11.1}_{-6.8} \times 10^{22}\,{\rm cm^{-2}}$ for the neutral absorber, with a covering fraction that varies between 0.16 and 0.48. The mildly and the highly ionized absorbers both almost fully cover the source (${\rm CF_{W1}} = 0.92^{+0.04}_{-0.05}$, ${\rm CF_{W2}} = 0.91^{+0.05}_{-0.08}$). The column density of the mildly ionized absorber is $N_{\rm H,W1} = 8.2^{+1.7}_{-1.1} \times 10^{21}\,{\rm cm^{-2}}$ with an ionization level that varies by more than an order of magnitude ($\log \xi_{\rm W1} = 0.14 - 1.28$). The highly ionized absorber with $N_{\rm H,W2} = 3.81^{+0.79}_{-0.43} \times 10^{22}\,{\rm cm^{-2}}$ shows a more moderate variability in the ionization level $\log \xi_{\rm W2} = 1.99 - 2.28$) throughout this observation.

However, the situation is different for Obs. 2+3. In these observations, which span ∼2.5 days in total, the neutral absorber shows no variations, fully covering the source with $N_{\rm H,N} = 1.62^{+0.53}_{-0.28} \times 10^{22}\,{\rm cm^{-2}}$. The best-fit suggests variable mildly ionized absorption. The different flux states require an absorber with $N_{\rm H,W1} = 7.83^{+0.97}_{-0.38} \times 10^{22}\,{\rm cm^{-2}}$, $\log \xi_{\rm W1} \sim 0.17 - 1.33$, and a covering fraction of $0.95^{+0.01}_{-0.02}$. As for the *NuSTAR* observation, we found a column density of the neutral absorber of $N_{\rm H,N} = 5.95^{+2.04}_{-0.91} \times 10^{22}\,{\rm cm^{-2}}$.

The thermal soft components (`apec`) are conservatively assumed to be constant for all observations (see Section 6 for more details about possible degeneracies and caveats in modeling the soft emission). The best-fit temperatures are 0.16 and 0.78 keV. The 0.5–2 and 3–10 keV fluxes of each emission component are listed in Table 5. The sum of the soft components (`apec1,2`) results in a flux of $\sim 5.6 \times 10^{-14}\,{\rm erg\,s^{-1}\,cm^{-2}}$ that is ∼1%–2% of the intrinsic power-law flux in the 0.5–2 keV range. We also note that the reflected flux is constant during all observations. The intrinsic

[19] We test the assumption of having a constant reflection component by fitting the spectra for each observation separately in the 5.5–8 keV range assuming a power law plus a Gaussian emission line. The `pexmin` normalization of the *NuSTAR* observation is tied to the one of Obs. 2+3. We found that the flux of the line is constant within each observation for all flux levels, and consistent between each observation.

[20] The ionization parameter is defined as $\xi = L_{\rm ion}/nr^2$, where n is the electron density of the gas and r is its distance from an ionizing source with 1–1000 Ry luminosity $L_{\rm ion}$.

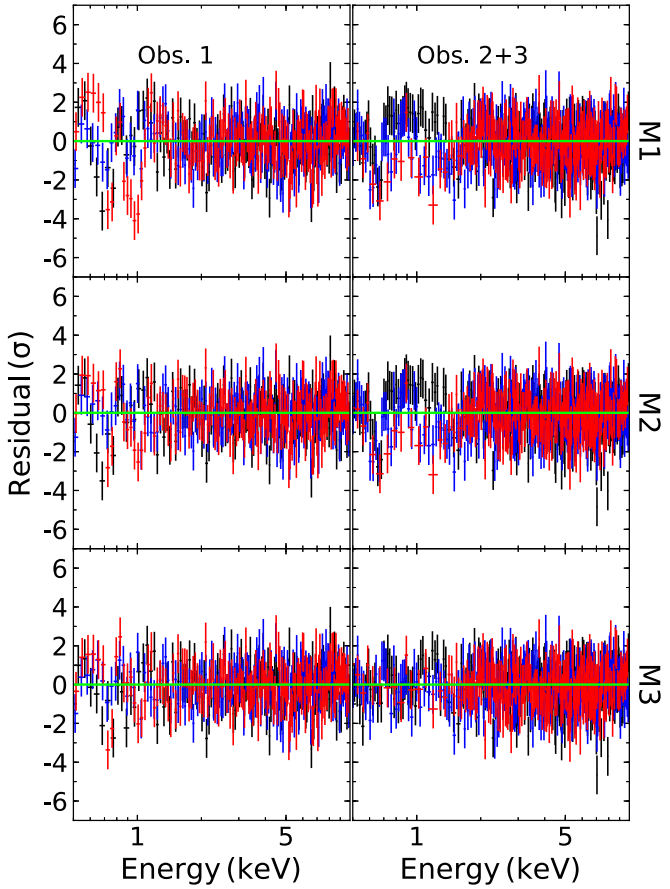

Figure 6. Residuals for the different models (M1–M3, top to bottom) obtained by adding various absorption/emission components (see text for details) for each *XMM-Newton* observation. The black, blue, and red spectra in each panel correspond to the low-, medium-, and high-flux spectra, respectively. The *NuSTAR* residuals are not shown because the added spectral components mainly affect the soft energies (below ∼2 keV).

unabsorbed power-law luminosity in the 3–10 keV range varies between 9.1×10^{39} and 2.4×10^{40} erg s^{-1}.

5. Discussion

We have analyzed multi-epoch *XMM-Newton* and *NuSTAR* flux-resolved spectra of the low-luminosity highly variable Seyfert galaxy NGC 4395. Our modeling suggests that the nuclear emission is obscured by three layers of absorption: neutral, mildly ionized, and highly ionized. The extent of intrinsic variability (a factor of ∼2.5) is revealed by the hard X-rays as probed by *NuSTAR* and cannot by itself account for all the flux variation (a factor of more than 10) that is observed in the soft X-rays (below 2 keV) during Obs. 1. To quantitatively estimate the expected variability within the context of our spectral modeling, we considered the best-fit model (M3) to simulate two sets of light curves. First, we removed all absorption components from M3, and created 2000 *XMM-Newton* light curves, with an exposure time of 1 ks each, assuming the best-fit parameters corresponding to Obs. 1. We considered the change in power-law normalization as being the only source of variability. We assumed a log-normal distribution of the power-law normalization that is consistent with the distribution of the 2–10 keV count rates. The black dash–dotted line in Figure 3 corresponds to the estimated $F_{\rm var}$ for this

Table 3
Best-fit Absorption Parameters

Parameter	Low	Medium	High
		Obs. 1	
$N_{\rm H,N}$		$34.36^{+11.09}_{-6.83}$	
$\rm CF_N$	$0.48^{+0.04}_{-0.07}$	$0.38^{+0.04}_{-0.05}$	0.16 ± 0.06
$N_{\rm H,W1}$		$0.82^{0.17}_{-0.11}$	
$\log \xi_{\rm W1}$	$0.14^{+0.19}_{-0.29}$	$0.67^{+0.09}_{-0.05}$	$1.28^{+0.09}_{-0.07}$
$\rm CF_{W1}$		$0.92^{+0.04}_{-0.05}$	
$N_{\rm H,W2}$		$3.81^{+0.79}_{-0.43}$	
$\log \xi_{\rm W2}$	$1.99^{+0.06}_{-0.19}$	$2.08^{+0.06}_{-0.09}$	$2.28^{+0.06}_{-0.11}$
$\rm CF_{W2}$		$0.91^{+0.05}_{-0.08}$	
		Obs. 2+3	
$N_{\rm H,N}$		$1.62^{+0.53}_{-0.28}$	
$\rm CF_N$		$1^{\rm fixed}$	
$N_{\rm H,W1}$		$7.83^{+0.97}_{-0.38}$	
$\log \xi_{\rm W1}$	$0.17^{+0.21}_{-0.17}$	$0.99^{+0.13}_{-0.35}$	$1.33^{+0.18}_{-0.11}$
$\rm CF_{W1}$		$0.95^{+0.01}_{-0.02}$	
		NuSTAR	
$N_{\rm H,N}$		$5.95^{+2.04}_{-0.91}$	
$\rm CF_N$		$1^{\rm fixed}$	

Note. Units are as follows: column densities in 10^{22} cm^{-2}, and ionization parameters in erg cm s^{-1}.

scenario. $F_{\rm var}$ is almost constant ($\langle F_{\rm var} \sim 0.3 \rangle$) over the full 0.4–10 keV range, except for a clear dip in the 6–7 keV range, characterized by the constant Fe line in the pexmon model. We repeated the same experiment by considering the best-fit M3 parameters from Obs. 2+3 and considering a constant neutral absorption with $N_{\rm H} = 1.6 \times 10^{22}$ cm^{-2}. The $F_{\rm var}$ estimated for both *XMM-Newton* and *NuSTAR* is shown in Figure 3 (dashed black lines and green dotted lines, respectively). The observed 0.4–1.5 keV band is dominated by the constant components (apec$_{1,2}$), which reduce the observed variability in this range. Above 1.5 keV, $F_{\rm var}$ follows a similar behavior to the previous set of simulations (with no absorption). Interestingly, a small decrease in the $F_{\rm var}$ is also seen in the ∼15–30 keV, corresponding to the Compton hump of the pexmon component. The simulations are in agreement with the measured $F_{\rm var}$ below 1 keV in Obs. 2+3 and above 4 keV for all observations. However, an excess in $F_{\rm var}$ can be seen in the 0.4–4 keV and 1–4 keV ranges in Obs. 1 and Obs. 2+3, respectively. We attribute this additional variability in Obs. 1 to independent (random) changes in the covering fraction of the neutral absorber and the ionization level of the ionized absorbers. This is consistent with the time-resolved spectral analysis (NR11) and PCA analysis (Parker et al. 2015) of Obs. 1.

As NR11 mentioned, the eclipse-like events seen in Obs. 1 could be either due to a single inhomogeneous cloud or to a system of different small clouds. The absorption variability might act on longer timescales compared to the intrinsic one, which will lead to a shift in the characteristic timescale toward lower values for higher energy ranges (as seen in Figure 4). As for Obs. 2+3, the neutral absorber shows no variations and fully covers the source, explaining the low variability level that is observed below 1 keV. We note that additional variability seen in the 1–4 keV range is probably due to changes in the ionization level of the mildly ionized absorber. The fact that the

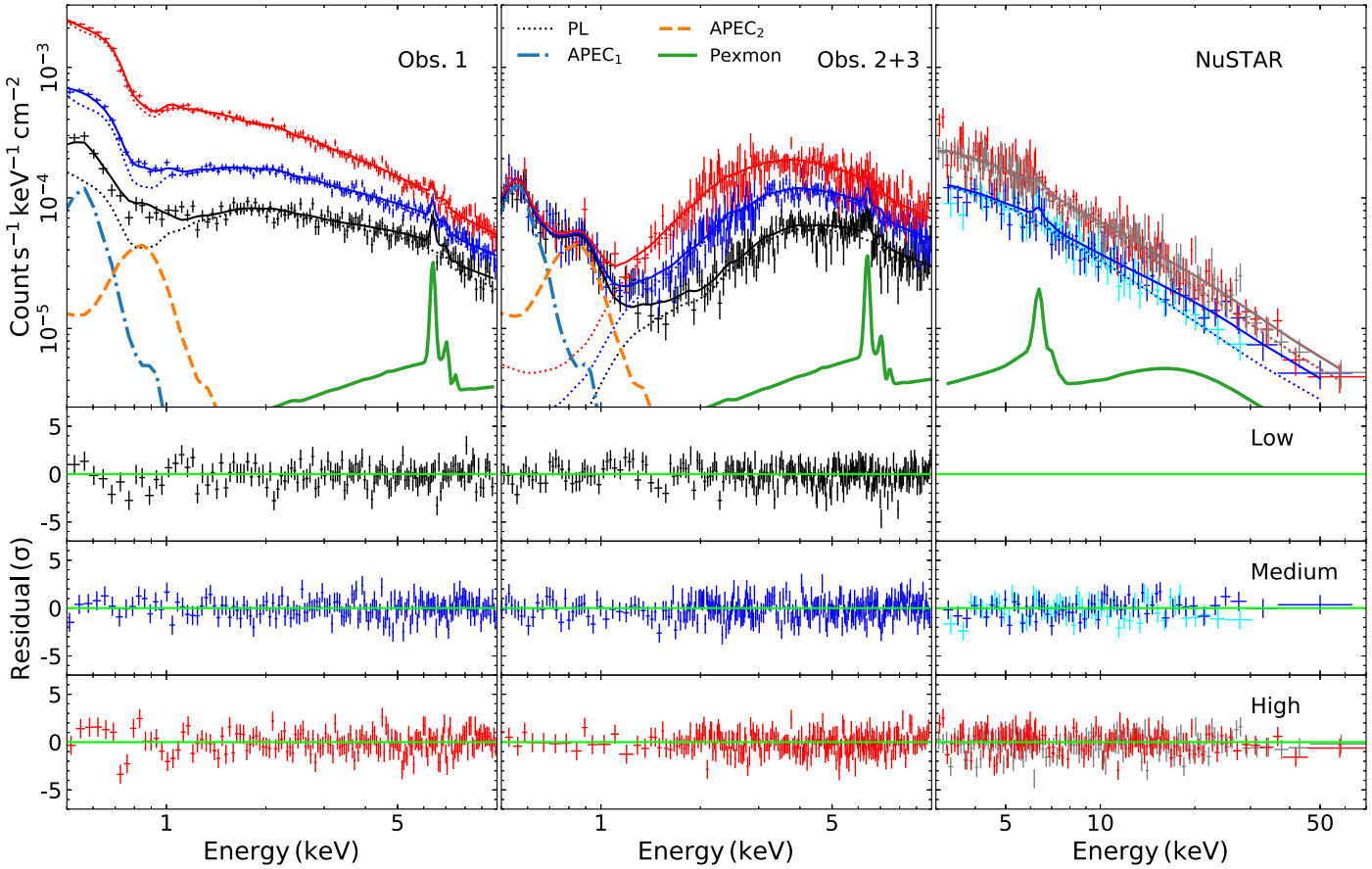

Figure 7. Top panel: spectra and best-fitting model (M3) for all observations. The black, blue, and red spectra in each panel correspond to the low-, medium-, and high-flux spectra, respectively. The blue/cyan and the red/gray *NuSTAR* spectra correspond to the medium- and high-flux FPMA/B spectra, respectively. The thin dotted lines represent the transmitted power-law component. The thick green lines represent the reflection component, the blue dash–dotted lines and the orange dashed lines correspond to the soft diffuse thermal emission components. Bottom panels: corresponding residuals for each flux level.

characteristic timescales are consistent at all energies in the PSDs of Obs. 2+3 might indicate that either (a) the intrinsic flux change and the ionization level changes are acting on similar timescales, or (b) the effects of the change in ionization level are smaller than those that are due to the intrinsic flux change and could not be identified by the current data quality.

We stress that the flux-resolved analysis presented in this work likely probes the full range of variability of the different components. This is complementary to the time-resolved analysis probing the succession of different states. This is more relevant for Obs. 1, which shows a more complex behavior than Obs. 2+3, where the neutral absorber shows no variability. Our results give the characteristic absorption/emission properties required by each flux state. In our approach, the flux levels are defined from the 2–10 keV band, which shows moderate variability because it is less affected by absorption compared to lower energies. Hence, any correlation between flux state and the obscuration level is not obvious a priori. For instance, the covering fractions of the neutral low- and medium-flux states in Obs. 1 are consistent. However, it could be possible that at high flux levels the gas becomes more ionized, hence the impact of neutral absorption diminishes. Testing this hypothesis requires an accurate identification of all ionization phases, tracking also the evolution of $N_{\rm H}$ and the covering fraction of each of them. This will be possible with the next generation of X-ray observatories. Any study of the absorber's structure and its evolution requires a time-resolved approach similar to NR11. We finally note that our results are qualitatively in agreement with the findings of NR11. The variability due to absorption

Table 4
Best-fit Parameters of Power Law, Thermal Emission (apec$_{1,2}$), and Reflection

Parameter	Low	Medium	High
kT_1		0.16 ± 0.01	
$\mathrm{Norm}_{\mathrm{apec1},-5}$		$5.46^{+1.29}_{-0.72}$	
kT_2		$0.78^{0.03}_{-0.06}$	
$\mathrm{Norm}_{\mathrm{apec2},-5}$		$1.61^{+0.13}_{-0.19}$	
		Obs. 1	
Γ		$1.67^{+0.02}_{-0.04}$	
$\mathrm{Norm}_{\mathrm{PL},-3}$	$1.12^{0.14}_{-0.12}$	$1.78^{+0.17}_{-0.16}$	$2.51^{+0.25}_{-0.21}$
$\mathrm{Norm}_{\mathrm{pexmon},-4}$		$8.28^{+0.69}_{-2.31}$	
		Obs. 2+3	
Γ		1.6 ± 0.04	
$\mathrm{Norm}_{\mathrm{PL},-3}$	$1.12^{+0.17}_{-0.04}$	$1.85^{+0.29}_{-0.03}$	$2.78^{+0.45}_{-0.09}$
$\mathrm{Norm}_{\mathrm{pexmon},-4}$		$6.61^{+2.37}_{-1.19}$	
		NuSTAR	
$\mathrm{Norm}_{\mathrm{PL},-3}$	...	$1.38^{+0.25}_{-0.05}$	$2.56^{+0.45}_{-0.10}$
$\mathrm{Norm}_{\mathrm{pexmon},-4}$		6.61^{tied}	

Note. The normalizations are in units of 10^{-3}, 10^{-5}, or 10^{-4} photon s^{-1} cm^{-2} keV^{-1}, as indicated by subscripts. Temperatures are in keV.

Table 5
Intrinsic (Unabsorbed) Fluxes in Units of 10^{-12} erg s^{-1} cm^{-2} for All the Emission Components in the 0.5–2/3–10 keV Ranges

	Low	Medium	High
Apec1		0.027/−	
Apec2		0.029−	
		Obs. 1	
Power law	2.59/3.82	4.07/6.01	5.79/8.56
Pexmon		−/0.37	
		Obs. 2+3	
Power law	2.65/4.47	4.41/7.45	6.66/11.26
Pexmon		−/0.41	
		NuSTAR	
Power law	⋯	−/5.59	−/10.03

is associated with the higher column density absorber (of about 10^{23} cm^{-2}). The lower column density absorber (of about 10^{22} cm^{-2}) is less variable, with the main difference compared to NR11 being that the current analysis finds that this absorber almost fully covers the source.

Interestingly, McHardy et al. (2016) found that the X-rays lead the UVW1 and the *g*-band light curves by 473 s and 788 s, respectively, during Obs. 2+3. This indicates that the UV/optical reprocessing region responding to the X-ray variability on these timescales is located at a distance that is closer to the BH than the BLR. This is consistent with thermal reprocessing by a standard accretion disk (see, e.g., Cackett et al. 2007; Kammoun et al. 2019). However, the current data quality does not allow us to identify any ionized reflection from the accretion disk in the X-ray spectra.

6. The Soft X-Ray Emission

We acknowledge that our modeling of the soft X-rays is limited by the low spectral resolution at low energies. We model the soft X-ray spectra by including two `apec` components. We associate the $\texttt{apec}_1$ component with the extended soft-emission regions seen in the *Chandra* and the *HST* [O III] images (see, e.g., Gómez-Guijarro et al. 2017). However, the nature of the $\texttt{apec}_2$ component is uncertain. This component could be the emission counterpart of the mildly ionized absorber or simply account for the gradient of temperature in the diffuse gas. But its presence might compensate for some inadequacy of the employed absorption (and emission) models (e.g., the residuals at ∼0.75 keV in the high-flux spectrum of Obs. 1). We also tested the possibility that the soft X-ray emission is due to a smooth soft component (modeled with a blackbody) that could be associated with the intrinsic disk emission given the low BH mass, in addition to a thermal diffuse emission (modeled with an `apec` component). This results in a statistically worse fit with $\chi^2/\mathrm{dof} = 1594/1530$ ($\Delta\chi^2 = +26$ for the same degree of freedom, dof). In fact, as the intrinsic X-ray emission is obscured, it would be natural that parts of the accretion disk (mainly the innermost region, which contributes most to the soft X-ray emission) are also obscured. However, it is impossible to identify the parts of the disk that are obscured and their covering fractions, knowing that the obscuring material has a complex and inhomogeneous structure. Overcoming the uncertainties in modeling the soft X-ray spectrum of this source requires higher spectral resolution, as will be provided by the next generation of X-ray missions. These missions would help us to accurately identify any thermal emission and/or absorption structures (see Section 6.3).

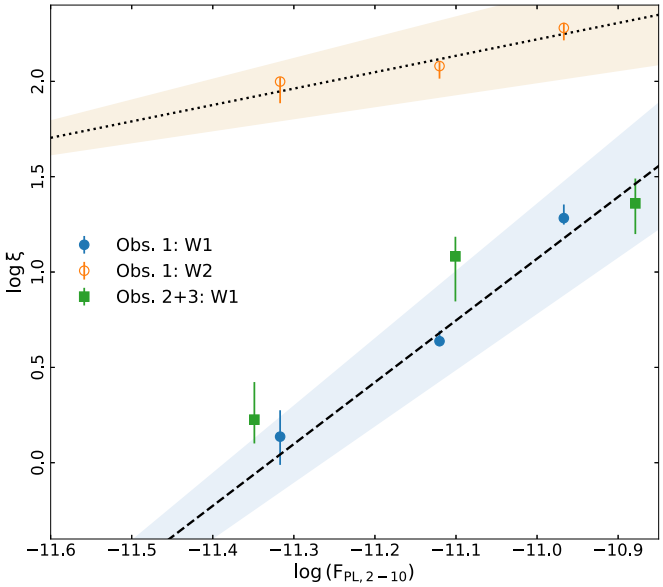

Figure 8. Best-fit ionization parameter (in units of erg cm s^{-1}) as a function of the power-law flux in the 3–10 keV band (in units of erg s^{-1} cm^{-2}), for all observations. The solid and dashed lines are the best-fit linear relation for Obs. 1 and Obs. 2+3, respectively. The error bars and the shaded regions correspond to the 1σ confidence level on the fitted ionization level and the linear relationship, respectively.

Table 6
The Distance of the BLR and the Sizes of the Obscuring Clouds Assuming Different Masses and Line Velocity Dispersions

$M_{\rm BH}$			$10^4\,M_\odot$	$3.6\times10^5\,M_\odot$
$R_{\rm BLR}$		10^{14} cm	$6.7\times10^4\,r_{\rm g}$	$1.9\times10^3\,r_{\rm g}$
Obs. 1 ($\delta t = 10$ ks)				
$D_{\rm C}$	$\sigma = 500$ km s^{-1}	5×10^{11} cm	333 $r_{\rm g}$	9.26 $r_{\rm g}$
	$\sigma = 1500$ km s^{-1}	1.5×10^{12} cm	1000 $r_{\rm g}$	28 $r_{\rm g}$
Obs. 2+3 ($\delta t > 220$ ks)				
$D_{\rm C}$	$\sigma = 500$ km s^{-1}	1.1×10^{13} cm	$7.3\times10^3\,r_{\rm g}$	200 $r_{\rm g}$
	$\sigma = 1500$ km s^{-1}	3.3×10^{13} cm	$2.2\times10^4\,r_{\rm g}$	611 $r_{\rm g}$

6.1. The Variable Ionized Absorption

Our results show that the ionized absorbers (both mildly and highly ionized) vary as a function of flux. We assume in our analysis that the variability is just in the ionization level of these components. We test the validity of this hypothesis by tying different pairs in the column density, ionization level, and covering fraction space, letting the third parameter free to vary. We found that letting the column density or the covering fraction free to vary results in statistically unacceptable fits with $\chi^2 = 1599$ and 1651 for 1530 dof, respectively, compared to $\chi^2 = 1568$ for a free ionization level with the same dof. Figure 8 shows the ionization level of the mildly (Obs. 1 and 2+3) and highly (Obs. 1 only) ionized absorbers as a function of the intrinsic power-law flux. This figure shows a clear positive correlation between the two quantities for the two absorbers. This may indicate that the ionized absorbers respond to the flux changes on timescales that are comparable to the intrinsic

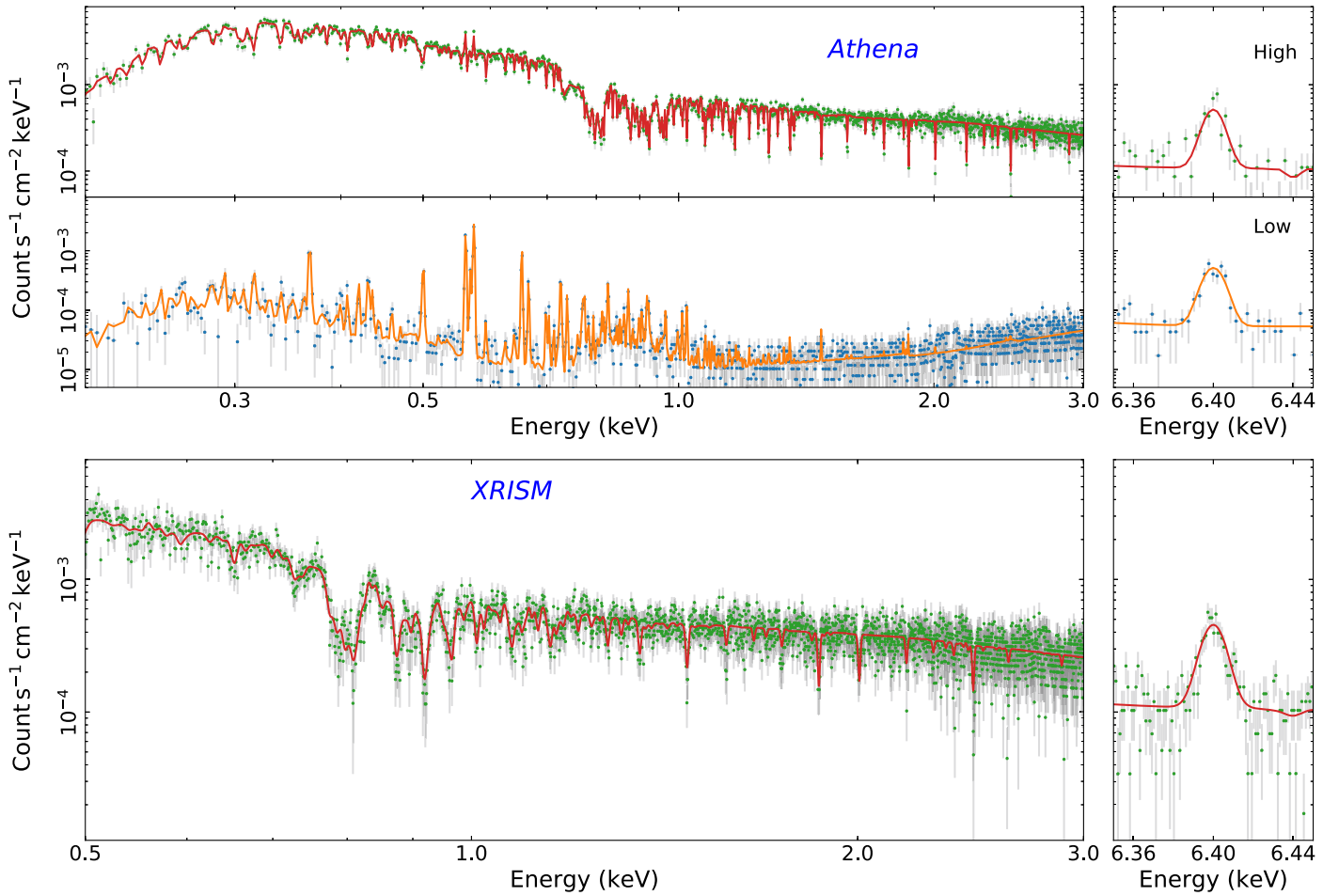

Figure 9. Top: simulated 10 ks *Athena*/X-IFU spectra of NGC 4395 assuming the high-flux Obs. 1 (upper row) and low-flux Obs. 2 (bottom row) best-fit models (solid lines). The spectra are binned using the "optimal" binning scheme (Kaastra & Bleeker 2016). Bottom: simulated 200 ks *XRISM*/Resolve spectra of NGC 4395 assuming the high-flux Obs. 1 best-fit model (red solid line). The RMF files are linearly compressed, which reduces the number of channels by a factor of 2. No grouping is applied to the spectra. The low-flux Obs. 2+3 state is dominated by the background, so we did not include it in the simulations. The left and right panels show the spectra below 3 keV and in the Fe Kα band, respectively.

variability timescale of the power-law emission. We fit the $\log \xi$ versus $\log F$ points for Obs. 1 and Obs. 2+3 together for the mildly ionized absorber (dashed line) and the highly ionized absorber (dotted line) assuming a linear correlation. The slopes of the correlations are 3.2 ± 0.3 and 0.9 ± 0.2 for the mildly and highly ionized absorbers, respectively. The slope of the highly ionized absorber is consistent with unity, as expected from the definition of the ionization parameter for a constant density and location. However, for the mildly ionized absorber, the slope of the correlation is larger than unity, which may indicate some change in the location and/or the density of the absorbing material. However, neither the size (hence the density derived from $N_{\rm H}$) nor the location of the gas could be well determined using the current data quality. We note that a similar relation between the ionization level and the intrinsic flux has been seen in other objects, for instance, NGC 4151 (Schurch & Warwick 2002; Zoghbi et al. 2019).

6.2. The BLR Size

The best-fit model suggests that the neutral reflection is constant in all observations. Thus, we can use this component as a tracer of the innermost extent of the cold obscuring material, assuming that it is responsible for the observed reprocessed emission. We added an `rdblur` relativistic blurring function to modify the `pexmon` component. This model assumes a Schwarzschild BH and a power-law emissivity profile ($\epsilon \propto r^{-q}$). We fixed the emissivity index at $q = 3$ and the outermost radius of the material at $10^6\, r_{\rm g}$ (where $r_{\rm g} = GM_{\rm BH}/c^2$ is the gravitational radius), considering a fixed inclination of 45°. We obtained a lower limit on the innermost radius $R_{\rm in} \gtrsim 4600\, r_{\rm g}$. This corresponds to 6.9×10^{12} cm or 2.5×10^{14} cm for $M_{\rm BH} = 10^4\, M_\odot$ or $M_{\rm BH} = 3.5 \times 10^5\, M_\odot$, respectively. The fit is driven mainly by the narrow Fe line, disfavoring a broader line profile hence lower value of $R_{\rm in}$. Using the ionization parameter definition ($\xi = L/nr^2$), we can obtain a rough estimate of the distance of the neutral material. Assuming an ionizing luminosity of $\sim 10^{41}$ erg s^{-1} and a density of 10^{9-11} cm^{-3}, we obtain $r \geqslant 10^{15-16}$ cm. This estimate is broadly consistent with the value obtained by blurring the reflection component, and with the typical size of the BLR ($R_{\rm BLR}$). In fact, Peterson et al. (2005) and Woo et al. (2019) determined a time lag of $\sim$1 hr and $\sim$1.4 hr for the C IV λ1549 and Hα emission lines, respectively, which gives $R_{\rm BLR} \sim 10^{14}$ cm. This corresponds to 6.7×10^4 (1.9×10^3) $r_{\rm g}$ for $M_{\rm BH} = 10^4\, (3.6 \times 10^5)\, M_\odot$.

The difference in the behavior of the neutral absorber between Obs. 1 (short-timescale variability) and Obs. 2+3 (constant over longer timescales) might indicate an

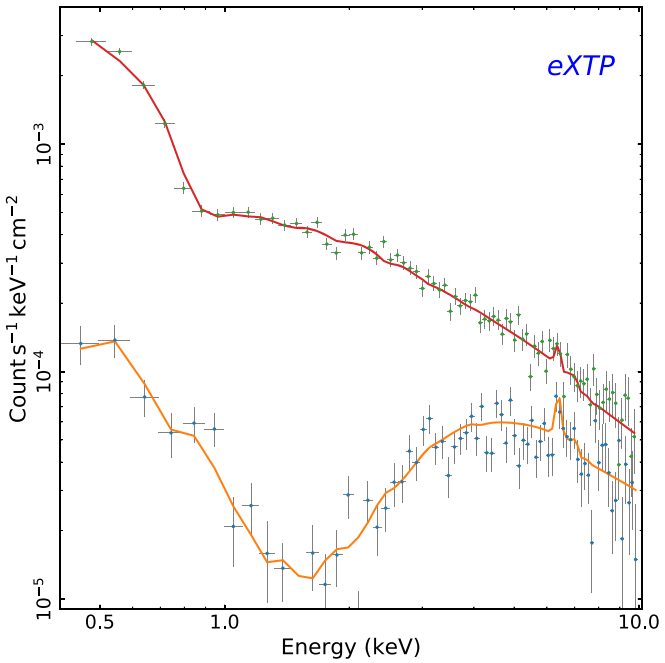

Figure 10. Same as Figure 9, but for the *eXTP*/SFA, with an exposure time of 1 ks for each spectrum. The spectra are binned using the "optimal" binning scheme.

inhomogeneous and layered BLR. A simple calculation can be made in order to have an estimate of the size of the obscuring neutral clouds. The variability timescale associated with the change in obscuration can be approximated as $\delta t \simeq D_{\rm C}/v$, where $D_{\rm C}$ is the characteristic size of the obscuring material, and v is the transverse velocity of the medium. Obs. 1 shows clear variations in the neutral obscuring material. NR11 argue that during this observation, the source exhibited eclipse-like events on timescales of ∼10 ks. This is also confirmed by our analysis, which shows variations in the covering fraction between the low-/medium-flux (0.48/0.38) states and the high-flux state (0.16). However, the neutral absorber remains constant and fully covers the source during Obs. 2+3. This can give us only a lower limit on the size of the obscuring material during these observations. The exact location and velocity of the obscuring material is unknown. Peterson et al. (2005) reported a velocity dispersion $\sigma \sim 1500\,{\rm km\,s^{-1}}$ for C IV, while Woo et al. (2019) reported a value of $\sigma \sim 426\,{\rm km\,s^{-1}}$ for the Hα line. Given this, and the uncertainty on the mass measurement, we estimate the cloud size assuming $v = 500$ and $1500\,{\rm km\,s^{-1}}$, and the two mass measurements reported in the literature, as shown in Table 6. The values are reported in cm and in $r_{\rm g}$. We assume a variability timescale of 10 ks for Obs. 1, while for Obs. 2+3 we can only estimate a lower limit on the size of the cloud, assuming $\delta t > 220$ ks. It is more likely that the absorber in Obs.1 is smaller, faster, and closer to the source than the absorber in Obs. 2+3. In these observations, the obscuration is most likely due to a slower and larger single cloud that is located at a larger distance. Assuming that the cloud density is $n_{\rm H} \sim N_{\rm H}/D_{\rm C}$, we derive densities of $\sim 2 \times 10^{11}\,{\rm cm^{-3}}$ for Obs. 1 (assuming $\sigma = 1500\,{\rm km\,s^{-1}}$) and $\sim 10^{9}\,{\rm cm^{-3}}$ for Obs. 2+3 (assuming $\sigma = 500\,{\rm km\,s^{-1}}$), given the best-fit $N_{\rm H,N}$ values listed in Table 3.

It is possible that the neutral absorption in principle could be related some outflowing material from the disk that could also extend to the BLR, as seen in NGC 5548, for example (Kaastra et al. 2014). In this case, it might be possible that the ionization state of the absorption in this source shows a radial dependence. Testing this would require high-resolution UV and X-ray spectra that would allow us to measure the ionization state of this material and energy shifts due to its motion. This would be possible with the next generation of X-ray observatories. The layered geometry, proposed in this work, is consistent with the general notion of a clumpy BLR and torus, as seen in several sources (Risaliti et al. 2005; Bianchi et al. 2012; Miniutti et al. 2014). The rapid changes seen in the neutral absorption during Obs. 1 are consistent with originating from the BLR. The lack of variability in the neutral absorption during Obs. 2+3 allows us to infer lower limits only. Hence, it is possible that the neutral material that obscures the source in these observations is located in the outer extent of the BLR or even in the torus (see, e.g., Miniutti et al. 2014).

6.3. Future Missions

Given the potential layering in the BLR inferred from our current analysis, future X-ray missions would help determine the low/moderate ionization state of the absorbers, which will allow us to better locate the different structures along the LOS, hence determining their orbital velocities and sizes. The high spectral resolution and sensitivity of future X-ray missions will allow us to identify many absorption and emission spectral features. This would be crucial for understanding the nature of the soft X-ray features: whether they are caused by a complex diffuse thermal emission or a smooth absorbed blackbody. Furthermore, future missions would enable a better understanding of the nature and the dynamics of the obscuring material and some better insights on outflows and AGN feedback. It would also be possible to identify the different ionization phases of the BLR gas and study the evolution of their absorbing columns and covering fractions. The bottom panel of Figure 9 shows a simulated 200 ks *XRISM*/Resolve[21] (Tashiro et al. 2018) spectrum based on the high-flux Obs. 1 best-fit model. The low-flux level of this source, based on our fits, would be comparable to the background level of the instrument. We stress that the simulated *XRISM* high-flux spectrum does not correspond to a 200 ks observation, but instead it observes the source in its highest flux state for this exposure, which will require a long monitoring. Instead, *XRISM* will allow us to study the Fe line profile even when the source is in its lowest flux state. This would allow us to determine the geometry and the location of the reprocessing material. In addition, it would help identify any disk reflection component and its possible eclipse.

Eclipsing events could be also studied by the enhanced X-ray Timing and Polarimetry mission (*eXTP*, Zhang et al. 2019). Thanks to the relatively large effective area of the Spectroscopic Focusing Array, we will be able to obtain spectra on timescales as short as 1 ks, as shown in Figure 10, though with low-energy resolution, which would be appropriate for the fast variability and the characteristic timescales for this source (see Section 3.2). For an eclipse timescale in the order of ∼10 ks, we will be able to probe the full evolution of the covering fraction. We also note that a crossing time $\delta t = 1$ ks would correspond to a distance of $\sim 2 \times 10^{4}\,r_{\rm g}$ or $560\,r_{\rm g}$ for $M_{\rm BH} = 10^{4}\,M_{\odot}$ or $3.6 \times 10^{5}\,M_{\odot}$, respectively.

[21] https://heasarc.gsfc.nasa.gov/docs/xrism/proposals/

Athena/X-IFU (Barret et al. 2018) would allow us to combine the time and energy resolution. The top panel of Figure 9 shows simulated 10 ks *Athena*/X-IFU spectra[22] based on the high-flux Obs. 1 and low-flux Obs. 2 best fits. X-IFU will allow us to study the variability in absorption on short timescales with high accuracy (see Barret & Cappi 2019, for more details about the ability of X-IFU to study absorption features in AGN). In addition, this will allow us to reveal any possible variability in the reflection spectrum, or broadening of the Fe Kα feature, which would help us to identify the location and the nature of the reprocessing material. High-resolution spectra would help in tracking any eclipsing events in NGC 4395, allowing us to probe the innermost region close to the BH (see Kammoun et al. 2018, for more details).

7. Conclusion

We have presented a detailed flux-resolved analysis of the X-ray spectra of NGC 4395 using multi-epoch non-simultaneous *XMM-Newton* and *NuSTAR* observations. Our results suggest that the source is affected by a complex structure of absorbing material. It consists of three layers with different ionization levels: neutral, mildly ionized, and highly ionized. The neutral material shows variations in its covering fraction during Obs. 1, which, in addition to the intrinsic variability, explains the high observed variability (a factor of $\sim$6) in the soft X-rays. However, this layer remains constant during Obs. 2 +3, where the variability is mainly intrinsic. The intrinsic variability could be also detected in the hard X-rays with *NuSTAR*. The ionization level of both mildly and highly ionized absorbers increases with the intrinsic flux, which indicates a response of the flux changes on timescales comparable to the intrinsic timescale. Our spectral modeling is also supported by the dependence of the PSD and $F_{\rm var}$ on energy. Future missions would allow us to study in detail the absorption/emission features in addition to the evolution of any absorption changes on their typical timescales.

We thank the anonymous referee for comments that improved the paper. This work made use of data from the *NuSTAR* mission, a project led by the California Institute of Technology, managed by the Jet Propulsion Laboratory, and funded by NASA, *XMM-Newton*, an ESA science mission with instruments and contributions directly funded by ESA Member States and NASA. This research has made use of the *NuSTAR* Data Analysis Software (NUSTARDAS) jointly developed by the ASI Science Data Centre (ASDC, Italy) and the California Institute of Technology (USA). The figures were generated using matplotlib (Hunter 2007), a PYTHON library for publication of quality graphics. The MCMC results were presented using the GetDist PYTHON package.

Facilities: NuSTAR, *XMM-Newton*.

Software: EMCEE (Foreman-Mackey et al. 2013), HEASoft (Nasa High Energy Astrophysics Science Archive Research Center (Heasarc), 2014), Matplotlib (Hunter 2007), NUSTARDAS (v1.8.0, https://heasarc.gsfc.nasa.gov/docs/nustar/analysis/, SAS (v17.0.0 Gabriel et al. 2004), XSPEC (Arnaud 1996), XSPEC_EMCEE (https://github.com/jeremysanders/xspec_emcee).

[22] http://x-ifu.irap.omp.eu/resources-for-users-and-x-ifu-consortium-members/

ORCID iDs

E. S. Kammoun https://orcid.org/0000-0002-0273-218X
E. Nardini https://orcid.org/0000-0001-9226-8992
A. Zoghbi https://orcid.org/0000-0002-0572-9613
E. M. Cackett https://orcid.org/0000-0002-8294-9281
M. T. Reynolds https://orcid.org/0000-0003-1621-9392
G. Risaliti https://orcid.org/0000-0002-3556-977X
D. Barret https://orcid.org/0000-0002-0393-9190
W. N. Brandt https://orcid.org/0000-0002-0167-2453
M. Koss https://orcid.org/0000-0002-7998-9581
R. F. Mushotzky https://orcid.org/0000-0002-7962-5446
J. Raymond https://orcid.org/0000-0002-7868-1622
D. Stern https://orcid.org/0000-0003-2686-9241

References

Arnaud, K. A. 1996, in ASP Conf. Ser. 101, Astronomical Data Analysis Software and Systems V, ed. G. H. Jacoby & J. Barnes (San Francisco, CA: ASP), 17
Barret, D., & Cappi, M. 2019, A&A, 628, A5
Barret, D., Lam Trong, T., den Herder, J.-W., et al. 2018, Proc. SPIE, 10699, 106991G
Barret, D., & Vaughan, S. 2012, ApJ, 746, 131
Belloni, T., Psaltis, D., & van der Klis, M. 2002, ApJ, 572, 392
Belloni, T., van der Klis, M., Lewin, W. H. G., et al. 1997, A&A, 322, 857
Bianchi, S., Maiolino, R., & Risaliti, G. 2012, AdAst, 2012, 782030
Blackburn, J. K. 1995, in ASP Conf. Ser. 77, Astronomical Data Analysis Software and Systems IV, ed. R. A. Shaw, H. E. Payne, & J. J. E. Hayes (San Francisco, CA: ASP), 367
Cackett, E. M., Horne, K., & Winkler, H. 2007, MNRAS, 380, 669
De Marco, B., Ponti, G., Cappi, M., et al. 2013, MNRAS, 431, 2441
Dewangan, G. C., Mathur, S., Griffiths, R. E., & Rao, A. R. 2008, ApJ, 689, 762
Filippenko, A. V., Ho, L. C., & Sargent, W. L. W. 1993, ApJL, 410, L75
Filippenko, A. V., & Sargent, W. L. W. 1989, ApJL, 342, L11
Foreman-Mackey, D., Hogg, D. W., Lang, D., & Goodman, J. 2013, PASP, 125, 306
Gabriel, C., Denby, M., Fyfe, D. J., et al. 2004, in ASP Conf. Ser. 314, Astronomical Data Analysis Software and Systems (ADASS) XIII, ed. F. Ochsenbein, M. G. Allen, & D. Egret (San Francisco, CA: ASP), 759
García, J., Dauser, T., Reynolds, C. S., et al. 2013, ApJ, 768, 146
García, J., & Kallman, T. R. 2010, ApJ, 718, 695
Gómez-Guijarro, C., González-Martín, O., Ramos Almeida, C., Rodríguez-Espinosa, J. M., & Gallego, J. 2017, MNRAS, 469, 2720
González-Martín, O. 2018, ApJ, 858, 2
Goodman, J., & Weare, J. 2010, Comm. App. Math. Comp. Sci., 5, 65
Harrison, F. A., Craig, W. W., Christensen, F. E., et al. 2013, ApJ, 770, 103
HI4PI Collaboration, Ben Bekhti, N., Flöer, L., et al. 2016, A&A, 594, A116
Hunter, J. D. 2007, CSE, 9, 90
Iwasawa, K., Fabian, A. C., Almaini, O., et al. 2000, MNRAS, 318, 879
Iwasawa, K., Tanaka, Y., & Gallo, L. C. 2010, A&A, 514, A58
Jansen, F., Lumb, D., Altieri, B., et al. 2001, A&A, 365, L1
Kaastra, J. S., & Bleeker, J. A. M. 2016, A&A, 587, A151
Kaastra, J. S., Kriss, G. A., Cappi, M., et al. 2014, Sci, 345, 64
Kammoun, E. S., Marin, F., Dovčiak, M., et al. 2018, MNRAS, 480, 3243
Kammoun, E. S., Papadakis, I. E., & Dočciak, M. 2019, ApJL, 879, L24
Kara, E., Alston, W. N., Fabian, A. C., et al. 2016, MNRAS, 462, 511
Karachentsev, I. D., & Drozdovsky, I. O. 1998, A&AS, 131, 1
Koliopanos, F., Ciambur, B. C., Graham, A. W., et al. 2017, A&A, 601, A20
Lira, P., Lawrence, A., O'Brien, P., et al. 1999, MNRAS, 305, 109
Matzeu, G. A., Reeves, J. N., Nardini, E., et al. 2016, MNRAS, 458, 1311
McHardy, I. M., Connolly, S. D., Peterson, B. M., et al. 2016, AN, 337, 500
McHardy, I. M., Koerding, E., Knigge, C., Uttley, P., & Fender, R. P. 2006, Natur, 444, 730
Mezcua, M., Civano, F., Marchesi, S., et al. 2018, MNRAS, 478, 2576
Miniutti, G., Sanfrutos, M., Beuchert, T., et al. 2014, MNRAS, 437, 1776
Moran, E. C., Eracleous, M., Leighly, K. M., et al. 2005, AJ, 129, 2108
Nandra, K., O'Neill, P. M., George, I. M., & Reeves, J. N. 2007, MNRAS, 382, 194
Nardini, E., & Risaliti, G. 2011, MNRAS, 417, 2571

Nasa High Energy Astrophysics Science Archive Research Center (Heasarc) 2014, HEAsoft: Unified Release of FTOOLS and XANADU, Astrophysics Source Code Library, ascl:1408.004
Parker, M. L., Fabian, A. C., Matt, G., et al. 2015, MNRAS, 447, 72
Peterson, B. M., Bentz, M. C., Desroches, L.-B., et al. 2005, ApJ, 632, 799
Reeves, J., Done, C., Pounds, K., et al. 2008, MNRAS, 385, L108
Risaliti, G., Elvis, M., Fabbiano, G., Baldi, A., & Zezas, A. 2005, ApJL, 623, L93
Schurch, N. J., & Warwick, R. S. 2002, MNRAS, 334, 811
Silva, C. V., Uttley, P., & Costantini, E. 2016, A&A, 596, A79
Smith, R. K., Brickhouse, N. S., Liedahl, D. A., & Raymond, J. C. 2001, ApJL, 556, L91
Strüder, L., Briel, U., Dennerl, K., et al. 2001, A&A, 365, L18
Tashiro, M., Maejima, H., Toda, K., et al. 2018, Proc. SPIE, 10699, 1069922
Vaughan, S. 2010, MNRAS, 402, 307
Vaughan, S., Edelson, R., Warwick, R. S., & Uttley, P. 2003, MNRAS, 345, 1271
Vaughan, S., Iwasawa, K., Fabian, A. C., & Hayashida, K. 2005, MNRAS, 356, 524
Whittle, P. 1953, ArM, 2, 423
Woo, J.-H., Cho, H., Gallo, E., et al. 2019, NatAs, 3, 755
Zhang, S., Santangelo, A., Feroci, M., et al. 2019, SCPMA, 62, 29502
Zoghbi, A., Miller, J., & Cackett, E. 2019, ApJ, 884, 26